

## Direct time-resolved observation of tungsten nanostructured growth due to helium plasma exposure

This content has been downloaded from IOPscience. Please scroll down to see the full text.

2015 Nucl. Fusion 55 033020

(<http://iopscience.iop.org/0029-5515/55/3/033020>)

View [the table of contents for this issue](#), or go to the [journal homepage](#) for more

Download details:

IP Address: 128.174.163.172

This content was downloaded on 14/03/2015 at 17:31

Please note that [terms and conditions apply](#).

# Direct time-resolved observation of tungsten nanostructured growth due to helium plasma exposure

P. Fiffis, D. Curreli and D.N. Ruzic

Center for Plasma Material Interactions, Department of Nuclear, Plasma and Radiological Engineering, University Illinois at Urbana-Champaign, Urbana, IL 61801, USA

E-mail: [fiffis1@illinois.edu](mailto:fiffis1@illinois.edu)

Received 9 October 2014, revised 11 December 2014

Accepted for publication 12 February 2015

Published 4 March 2015



CrossMark

## Abstract

Determination of the mechanisms underlying the growth of tungsten fuzz is an important step towards mitigation of fuzz formation. Nanostructured tungsten was produced on resistively heated tungsten wires in a helicon plasma source (maximum flux of  $2.5 \times 10^{21} \text{ m}^{-2} \text{ s}^{-1}$ ). Asymmetry in the setup allows for investigation of temperature and flux effects in a single sample. An effort at elucidating the mechanism of formation was made by inspecting SEM micrographs of the nanostructured tungsten at successive fluence steps of helium ions up to a fluence of  $1 \times 10^{27} \text{ m}^{-2}$ . To create these micrographs a single tungsten sample was exposed to the plasma, removed and inspected with an SEM, and replaced into the plasma. The tungsten surface was marked in several locations so that each micrograph is centred within 200 nm of each previous micrograph. Pitting of the surface (diameter  $9.5 \pm 2.3 \text{ nm}$ , fluence  $(5 \pm 2) \times 10^{25} \text{ m}^{-2}$ ) followed by surface roughening (fluence  $(9 \pm 2) \times 10^{25} \text{ m}^{-2}$ ) and tendrill formation (diameter  $30 \pm 10 \text{ nm}$ , fluence  $(2 \pm 1) \times 10^{26} \text{ m}^{-2}$ ) is observed, providing evidence of bubble bursting as the mechanism for seeding the growth of the tungsten fuzz.

Keywords: tungsten fuzz, divertor material, bubbles and blisters

(Some figures may appear in colour only in the online journal)

Under irradiation by helium plasmas, tungsten surfaces at elevated temperatures have shown evidence of nanostructuring [1]. At temperatures between 1000 and 2000 K, and at fluxes in excess of  $2 \times 10^{20} \text{ m}^{-2} \text{ s}^{-1}$ , this nanostructuring takes the form of nanotendrils colloquially referred to as ‘tungsten fuzz’ [2]. The tungsten surfaces in the International Thermonuclear Experimental Reactor (ITER) will be exposed to large helium fluxes at high temperature [3, 4]. This has prompted further investigation into the formation of tungsten fuzz in tokamaks. Studies have demonstrated fuzz formation in fusion devices [2]. Traditionally, tungsten fuzz has been produced in linear plasma devices capable of delivering large fluxes at elevated temperatures [5–7]. However, a recent study has demonstrated fuzz formation in a smaller test stand under exposure from a helicon plasma [8]. To date, most of these experiments expose a single sample to a single flux at a single temperature, and therefore studies can only show fluence/flux steps at a set temperature. A unique geometry employed at the University of Illinois allows for the exposure of a single sample of tungsten wire wound around an alumina tube to a helicon plasma. Due to the geometry, the wire is exposed to a variety of fluxes and a range of temperatures.

The experimental setup consists of a MORI 200 helicon plasma source [9] and a resistively heated tungsten wire

mounted on an alumina tube. The helicon plasma for the exposures detailed herein was run at an RF power of 700 W, a helium pressure of 100 mTorr, and a magnetic field of 120 G. RF compensated Langmuir probe measurements of the plasma return a density of  $(1.0 \pm 0.3) \times 10^{18} \text{ m}^{-3}$  and a temperature of  $4 \pm 1.5 \text{ eV}$  in the region where the sample was placed [10]. The sample consists of a 0.5 mm diameter tungsten wire (extruded, annealed, 99.95%, Alfa Aesar). The sample is passed through and then wound around an alumina tube. A photo of the wire and a circuit diagram are shown in figure 1. To achieve temperatures necessary for fuzz formation a current was passed through the wire to heat it. This configuration was chosen so that the tungsten surface exposed to the plasma would have a broad temperature profile. The wire was then biased to a negative voltage with respect to plasma potential. In this case, the wire was biased at 40 V below plasma potential resulting in 40 eV helium ions at a flux of  $2.5 \times 10^{21} \text{ m}^{-2} \text{ s}^{-1}$  which is well within the range of ions used for the production of nanostructured tungsten on linear plasma devices [11]. Scanning electron microscopy (Hitachi S-4700) is performed on the samples after exposure to the helium plasma. The tungsten wire was indented in multiple locations with a diamond bandsaw to recover images of the same location on an SEM tool in between fluence

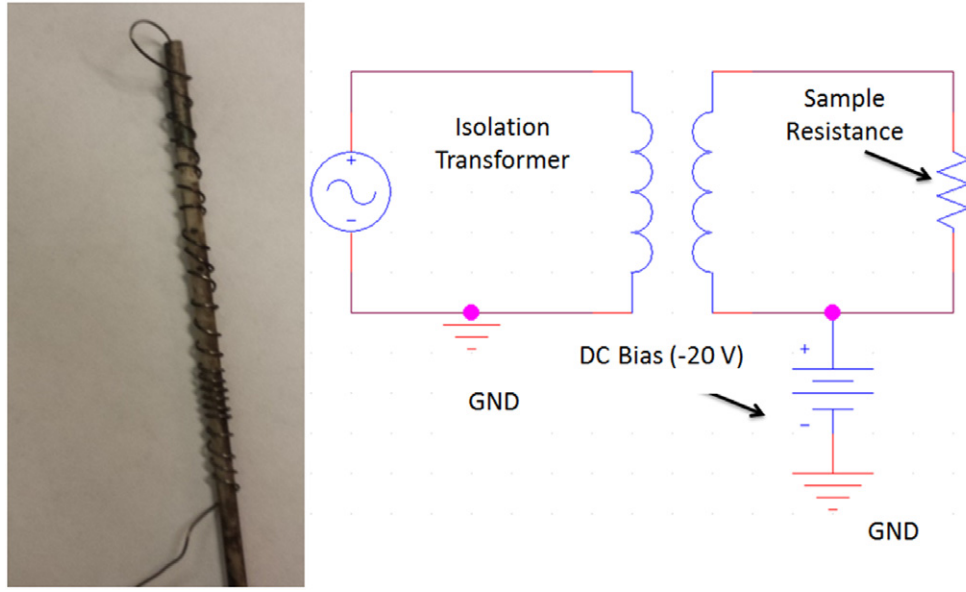


**Figure 1.** (left) Photograph of sample showing tungsten wire wrapped around alumina tube (wire diameter is 0.5 mm). (right) Circuit diagram of heating circuit for tungsten wire illustrating a Variac driving an isolation transformer which passes a current through the tungsten wire, which is also biased to  $-20$  V with the assistance of a dc power supply.

steps. This allowed for tracking the evolution of the tungsten surface as the tungsten fuzz developed. A SEM micrograph of fuzz produced at a flux of  $2.5 \times 10^{21} \text{ m}^{-2} \text{ s}^{-1}$ , a fluence of  $1.2 \times 10^{27} \text{ m}^{-2}$  and a temperature of 1500 K is shown in figure 2, the thickness of this fuzz layer was 600 nm. While similar fluences have been shown [1, 7, 11] to grow microns of nanostructure, the reduced thickness is consistent with observations of reduced fuzz growth rate at fluxes below  $7 \times 10^{21} \text{ m}^{-2} \text{ s}^{-1}$  [12]. Temperatures of the sample were obtained from a calibrated finite difference heat transfer model comprising the input power from helium ions and resistive heating, and output power through radiation and conduction, including coupling of the tungsten wire to the alumina tube via conduction and radiation. The model results, analysed across several samples, are consistent with the transition temperature in the literature [13]. Fuzz is produced in regions at 1100 K, but not in regions at 900 K, as can be seen in the comparison in figure 3.

SEM images taken of a single location over multiple fluence steps are shown in figures 4 and 5, illustrating the evolution of the nanostructure at temperature  $T = 1150 \pm 100$  K. Plasma conditions are  $n_e = (1 \pm 0.3) \times 10^{18} \text{ m}^{-3}$ ,  $T_e = 4 \pm 1.5$  eV. Figure 4 is the unaltered SEM micrographs, while figure 5 uses the same micrographs only zoomed and rotated. The triangle and lines in all the images in figure 5 were a marker to indicate the correct rotation and location to rectify imprecision in sample placement and rotation in the SEM and are included as a visual cue to illustrate the growth of individual tendrils. In the sequence of micrographs, it can be seen that the process begins with pitting of the surface ( $\Phi_{\text{He}} < 5 \times 10^{25} \text{ m}^{-2}$ , figures 3(a)–(c), more clearly in figures 4(a)–(c)). This is proposed to be due to helium bubble formation in the bulk and diffusion to the surface. When these bubbles hit the surface, the top delaminates, forming voids or holes. These holes have a diameter of  $9.5 \pm 2.3$  nm in diameter. Migration of helium bubbles causes the pitting of

the surface to an areal density of approximately  $875 \pm 30$  pits  $\mu\text{m}^{-2}$  before statistic variation to the number and location of the voids being formed begins to create hillocks and valleys (areal density  $40 \pm 10$  hillocks  $\mu\text{m}^{-2}$ , peak separation distance  $90 \pm 35$  nm, hill diameter  $67 \pm 26$  nm). This is observed as the fluence progresses ( $5 \times 10^{25} \text{ m}^{-2} < \Phi_{\text{He}} < 2 \times 10^{26} \text{ m}^{-2}$ , figures 3(d) and (e)). As time progresses, there exists a shorter path for bubbles to reach the surface in the valleys as opposed to the hillocks, and a random walk model of bubble movement would then imply more bubbles delaminating in the valleys and sides rather than at the top of the hillocks, causing sharpening of the hillocks ( $2 \times 10^{26} \text{ m}^{-2} < \Phi_{\text{He}} < 4 \times 10^{26} \text{ m}^{-2}$ , figures 3(f) and (g)). The distribution of hillock diameters begins to narrow as well (hill diameter  $42 \pm 8$  nm). Eventually, the hillocks become tendril-like in nature, maintaining diameters of 30–40 nm ( $4 \times 10^{26} \text{ m}^{-2} < \Phi_{\text{He}} < 6 \times 10^{26} \text{ m}^{-2}$ , figure 3(h)). As fluence increases beyond this step, the tendrils continue to rise out of the bulk, due to the path length from bubble generation to bubble rupture being shorter to the valleys than the top of the tendrils, leading to the growth of the tungsten fuzz ( $6 \times 10^{26} \text{ m}^{-2} < \Phi_{\text{He}}$ , figures 3(i) and (j)). This hypothesis is consistent with that of Kajita [13], where bubble bursting is assumed to be the mechanism for initial roughening of the surface, and further growth of nanostructures is hypothesized to be from nonuniform impact of bubbles rising to the surface. Additional studies [14, 15] support the importance of bubble formation in the growth of nanostructured tungsten.

A simple Monte Carlo/random walk computational model was constructed to support this hypothesis. The sole tenant of this model is that if bubbles are formed in bulk and impact the surface, that they are more likely to burst in a depression than a raised feature. It makes no assumptions nor draws any conclusions about helium clusters [16] and helium bubble growth [17], tungsten relocation via bubble rupture/loop punching [18], bubble transport from the bulk to the surface, or bubble transport inside individual tendrils. The model aims to

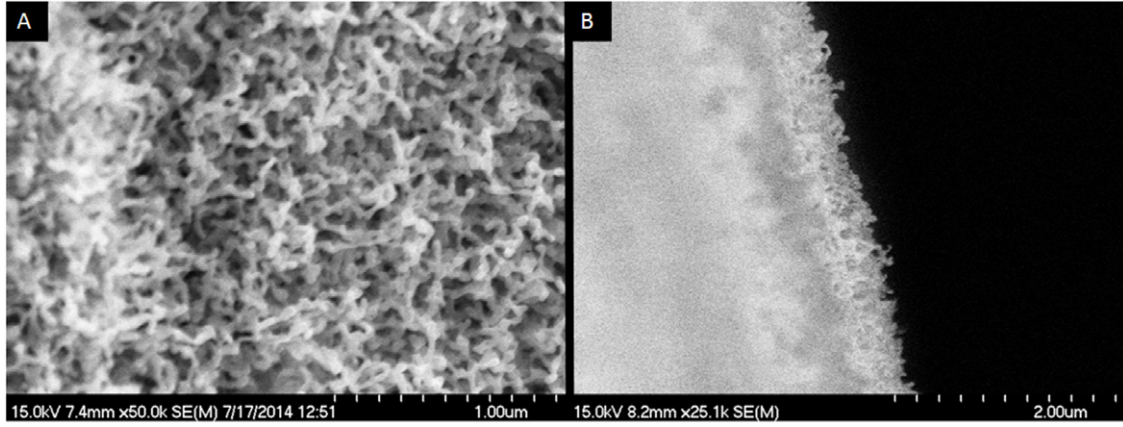


**Figure 2.** Nanostructured tungsten produced by a helicon source at Illinois. Top down view of fuzz can be seen at left with tendrils similar to those seen in linear plasma devices. Thickness can be measured from view of side of wire with fuzz thickness approximately 600 nm. Scale of  $1\ \mu\text{m}$  in (a) is for the full hash mark set (each hash mark of the ten is for 100 nm).

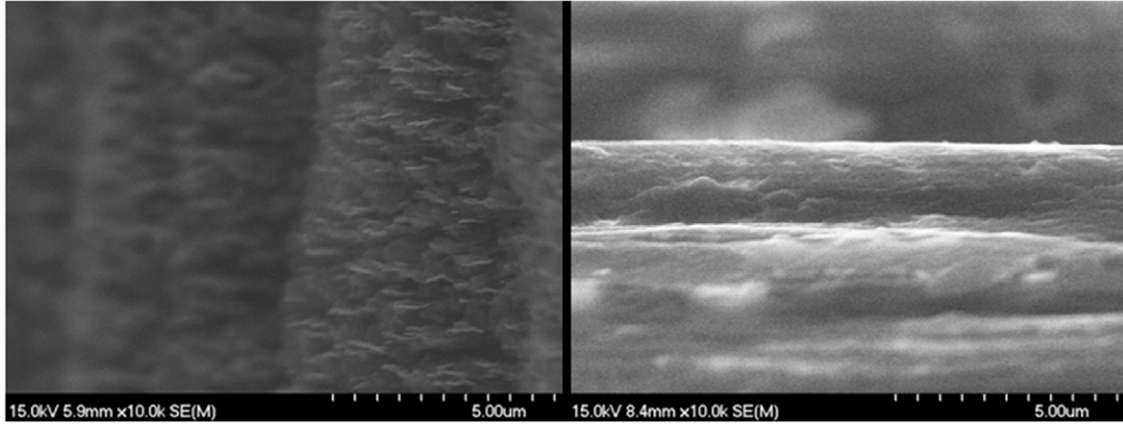


**Figure 3.** Comparison between two locations on a single sample irradiated at 1100 K (left) and 900 K (right). Appearance of nanostructuring in left micrograph as opposed to none in the right micrograph is evidence of reasonable calibration of thermal model.

recreate the initial morphological changes (pitting formation), assuming that a bubble has reached the surface, without including a temperature dependence or material properties. The model involves two lattices, or planes, one to represent the surface and another to represent the bulk. Bubbles are generated on the bulk plane at randomly chosen lattice point  $(i_0, j_0)$  with a diameter of 10 nm, set by the inter-lattice point separation distance and equal to that of the experimentally observed pits. The computational domain employed here used  $100 \times 100$  lattices, corresponding to a  $1\ \mu\text{m}$  by  $1\ \mu\text{m}$  area. These bubbles are randomly ‘walked’ to the top plane by assuming that the probability of a bubble impacting in a given location is a Gaussian distribution over the path length, the longer the path, the lower the probability:

$$P_{i,j} = \frac{e^{-\frac{d^2}{a^2}}}{\sum_{i,j} e^{-\frac{d^2}{a^2}}}, d^2 = a^2 ((i - i_0)^2 + (j - j_0)^2) + h_{i,j}^2$$

where  $a$  is the bubble diameter,  $h$  the surface height at lattice location  $(i, j)$ , and  $d$  is the distance between bubble generation and bubble impact. Due to this, bubbles are more likely to hit in depressed features rather than raised features. Once a bubble impacts the top plane, the height of the top plane in the cell where it hits is decreased and the height is

increased in the neighbouring cells, altering the path length for the next bubble while conserving volume:  $h_{i,j} = h_{i,j} - 1$ ,  $h_{i\pm 1,j} = h_{i\pm 1,j} + .1476$ ,  $h_{i,j\pm 1} = h_{i,j\pm 1} + .1476$ ,  $h_{i\pm 1,j\pm 1} = h_{i\pm 1,j\pm 1} + .1024$ . Figure 6 shows a diagram as well as an example model result. This simple model recreates well the initial pitting of the surface, saturating at approximately 600–1000 pits  $\mu\text{m}^{-2}$  before further texturing, in agreement with the experimental result of  $875 \pm 30$  pits  $\mu\text{m}^{-2}$ . As in the experiment, this is followed by creation of hills and valleys, which the model predicts to have an areal coverage (areal density in hills  $\mu\text{m}^{-2}$  multiplied by area/hill) of approximately  $2 \times 10^5\ \text{nm}^2\ \mu\text{m}^{-2}$ , again in agreement with the experimental result of  $(1.4 \pm 1) \times 10^5\ \text{nm}^2\ \mu\text{m}^{-2}$ . Growth of tendrils from the surface subsequently commences. Growth of these tendrils is preceded by a narrowing of the hills, also predicted by a reduction in areal coverage in the model to approximately  $8 \times 10^4\ \text{nm}^2\ \mu\text{m}^{-2}$ , which falls within the error bars of the experimental result of  $(5.5 \pm 4) \times 10^4\ \text{nm}^2\ \mu\text{m}^{-2}$ , illustrated in figure 7 via a graph of areal coverage. The cumulative height distribution of the cells exhibits two inflection points, one indicating growth above the surface, and one recession of features into the surface. The areal coverage,  $A_c$  was calculated from the model by summing the area,  $A_i$  of all cells having



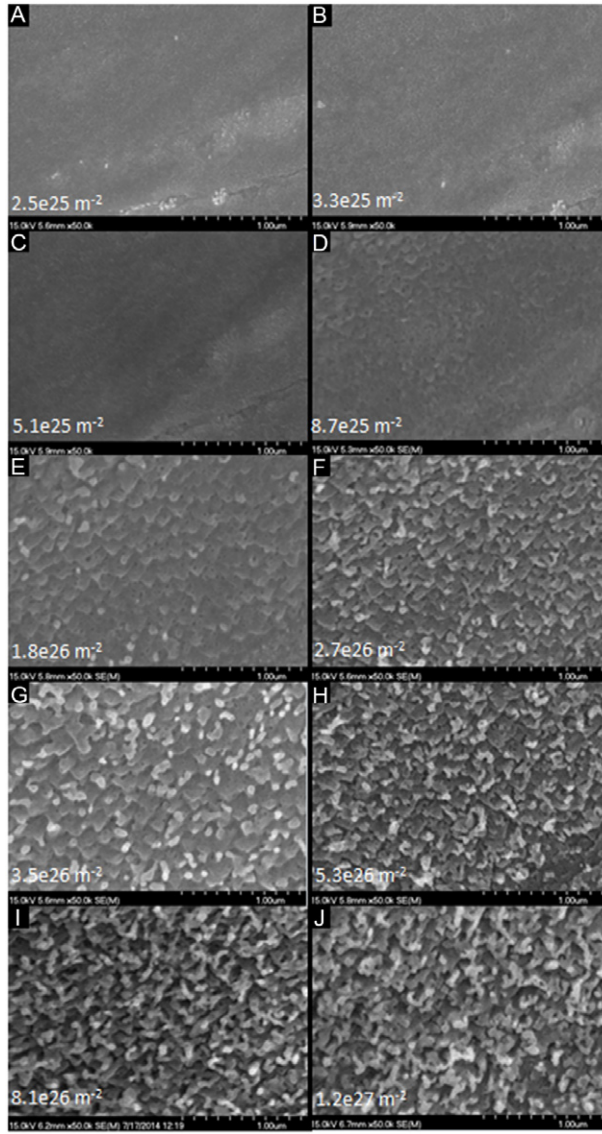


**Figure 4.** Temporal (and therefore fluence) evolution of nanostructures at 1150 K. (a)–(c) show the appearance of pits in the surface (more evident in figure 5). (d) and (e) show continued roughening of the surface leading to the onset of hill and valley formation. (f) and (g) illustrate continued ‘pitting’ of the surface from bubble rupture, which we hypothesize leads to narrowing of the hills. In (h)–(j) the narrowed hills continue to grow from the surface as the onset of fuzz formation.

height  $h_i$  above a critical height,  $h_{\text{crit}}$ .  $A_c = \sum_i A_i$  where

$$A_i \begin{cases} A_i \neq 0 & \text{if } h_i > h_{\text{crit}} \\ A_i = 0 & \text{if } h_i < h_{\text{crit}} \end{cases}$$

where  $h_{\text{crit}}$  is determined by the upper inflection point in the cumulative height distribution:

$$\left. \frac{d}{dH^2} \left( \sum_j \sum_{-\infty}^H h_j < H \right) \right|_{H=h_{\text{crit}}} = 0.$$

The critical height,  $h_{\text{crit}}$ , varies with fluence and is a clear indicator of what has grown out of the surface and what has not. Assuming the bubble formation rate to be linearly proportional

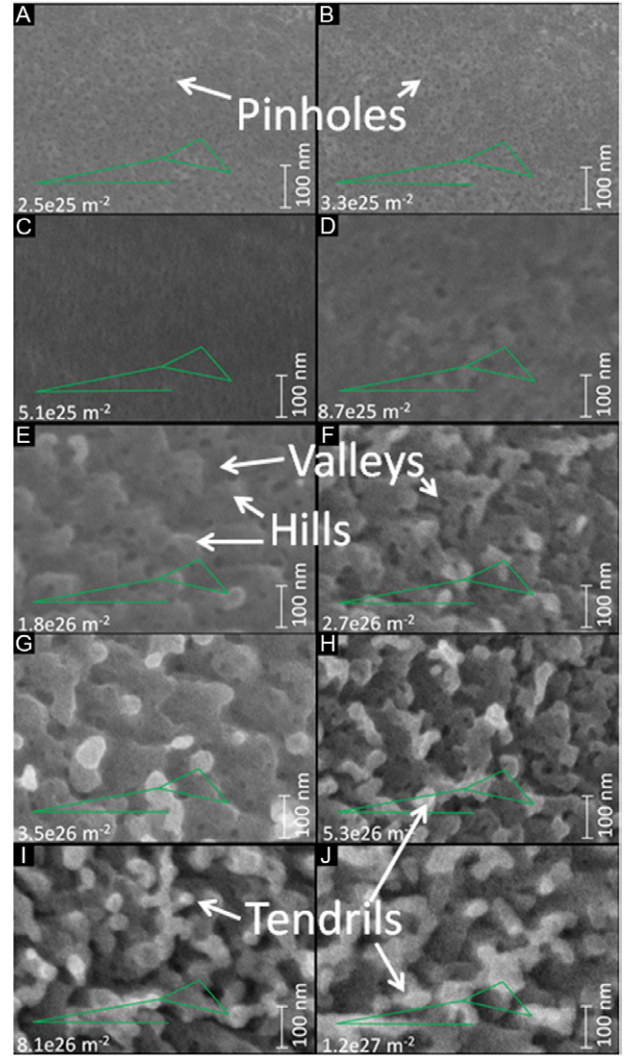


**Figure 5.** Zoomed, rotated and aligned micrographs of figure 3. Green lines used as both visual cue and method of alignment. Evolution and growth of individual tendrils of approximately 30–40 nm in diameter is evident.

to helium fluence at small thicknesses of fuzz, and setting 1000 bubbles equal to a fluence of  $5 \times 10^{25} \text{ m}^{-2}$  (pitting saturation occurring at  $<1000$  bubbles in the model and approximately  $5 \times 10^{25} \text{ m}^{-2}$  experimentally), the model predicts hill growth between fluences of  $1.5 \times 10^{26}$  to  $4 \times 10^{26} \text{ m}^{-2}$ . It then predicts hill sharpening and eventual fuzz growth at fluences greater than  $4 \times 10^{26} \text{ m}^{-2}$ , similar to those measured experimentally. Finally, a measurement of the radial distribution function of the tendrils from the model suggests an inter-tendrils separation of 50–60 nm which roughly agrees with the experimentally obtained inter-tendrils separation of  $90 \pm 35 \text{ nm}$ . Table 1 is a summary of these comparisons. A series of plots of the surface height over time from the model is shown in figure 8 such that it complements the progression of figure 5.

## 1. Discussion and summary

The experimental results detailed here mark for the first time, to the knowledge of the authors, the observation of individual nanostructured tendrils at progressive fluence levels

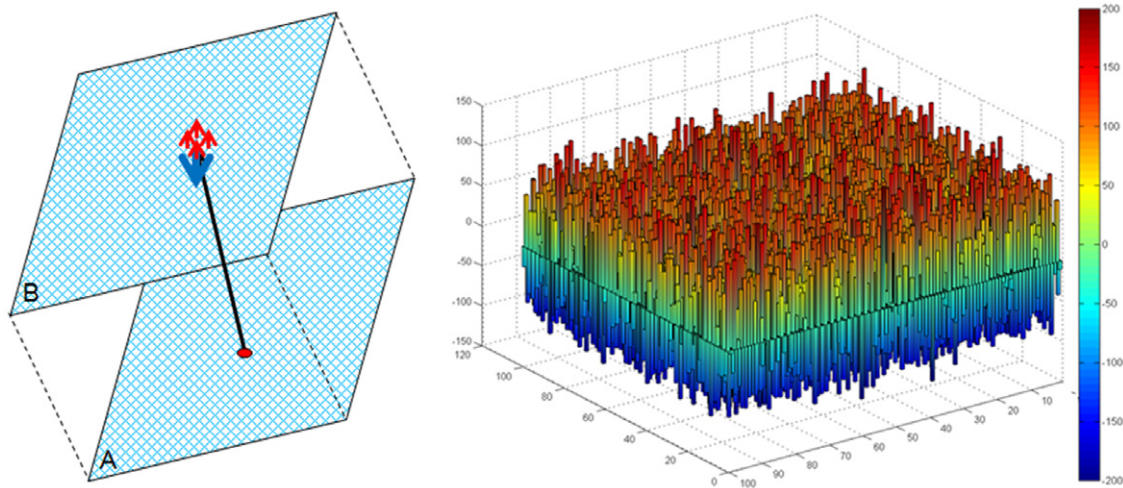


**Figure 6.** (left) Schematic of fuzz growth model showing bubble generation in plane A (bulk plane), impact in plane B (surface plane) and modification of the surface height (blue arrow illustrating decrement and red arrows incrementing of adjacent cells). (right) Side view of model nano-‘fuzz’, in units of 10 nm at simulation end (beginning of tendril growth phase). Tendril growth and bulk recession can be readily observed.

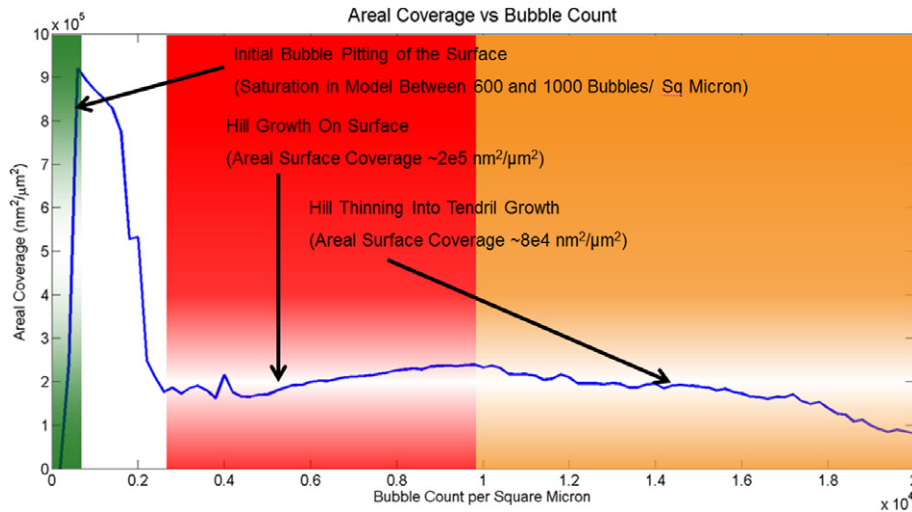


**Figure 7.** Areal coverage of nanostructure features versus bubble count. Curve progresses through initial pitting of the surface to a bubble count of 600–1000 bubbles per square micron (highlighted in green) before further nanostructuring of the surface. Hillock growth (highlighted in red) follows reaching a maximum areal coverage of about  $2 \times 10^5 \text{ nm}^2 \mu\text{m}^{-2}$  before gradually thinning into nanostructured tendrils (highlighted in orange) reaching.

**Table 1.** Comparison of morphological data from experiment and model. The only free parameter of impact in the model is that 1000 He bubbles result from a fluence of  $5 \times 10^{25} \text{ He}^+ \text{ m}^{-2}$ .

Experimental observation	Model analogue	Experimental fluence	Model fluence (scaled to match pitting threshold)
Pitting of surface saturates at $875 \pm 30 \text{ pits } \mu\text{m}^{-2}$	Pitting of surface saturates between 600 and 1000 pits $\mu\text{m}^{-2}$	$5 \times 10^{25} \text{ m}^{-2} \text{ He}^+ \text{ ions}$	$5 \times 10^{25} \text{ m}^{-2} \text{ He}^+ \text{ ions}$
Hill areal coverage $(1.4 \pm 1) \times 10^5 \text{ nm}^2 \mu\text{m}^{-2}$	Hill areal coverage $2 \times 10^5 \text{ nm}^2 \mu\text{m}^{-2}$	$5 \times 10^{25} - 2 \times 10^{26} \text{ m}^{-2} \text{ He}^+ \text{ ions}$	$1.5 \times 10^{26} - 4.5 \times 10^{26} \text{ m}^{-2} \text{ He}^+ \text{ ions}$
Tendril thinning and growth, areal coverage $(5.5 \pm 4) \times 10^4 \text{ nm}^2 \mu\text{m}^{-2}$	Tendril thinning and growth, areal coverage $8 \times 10^4 \text{ nm}^2 \mu\text{m}^{-2}$	$> 2 \times 10^{26} \text{ m}^{-2} \text{ He}^+ \text{ ions}$	$> 4.5 \times 10^{26} \text{ m}^{-2} \text{ He}^+ \text{ ions}$
Inter-tendril separation $90 \pm 35 \text{ nm}$	Inter-tendril separation 50–60 nm	—	—

on the same sample. The series of micrographs presented herein shows an evolution of a tungsten surface that first shows evidence of pitting at low fluences, followed by further deformation into a series of hills and valleys that progress to form the tungsten nanotendrils. The experimental findings

support the theory of Kajita *et al* [13], as well as provide a benchmark that may be used for validation of morphologies predicted by computational codes.

The much simpler computational model employed here serves to test the hypothesis detailed at the end of the



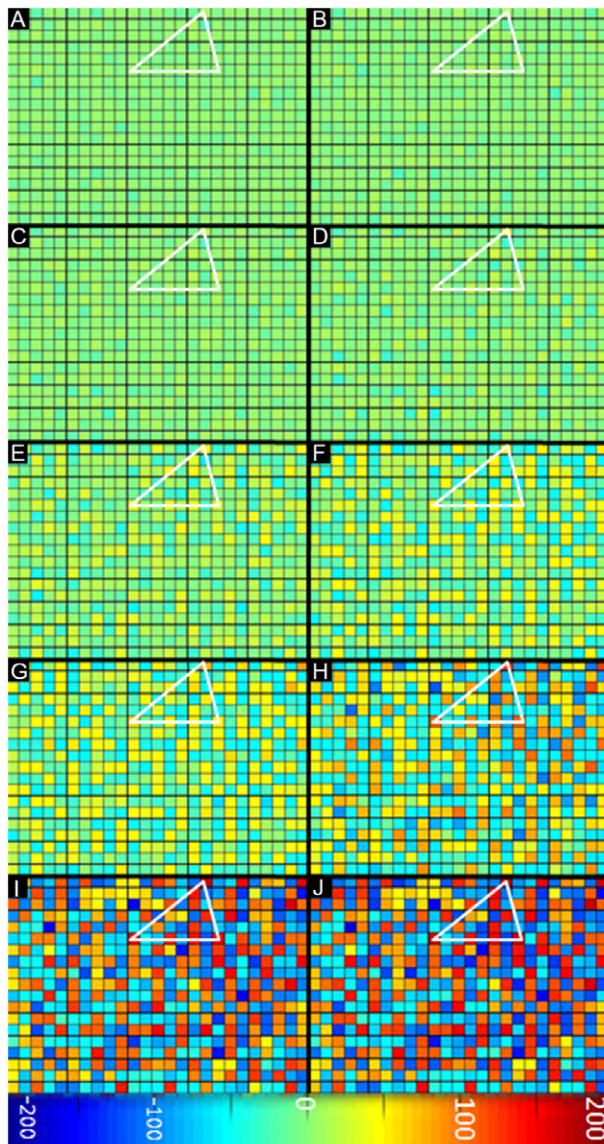


**Figure 8.** Computational model results presented as analogue of micrographs in figure 4. Again, a triangle (white), is used as a visual cue to show evolution of individual nanostructures. Similar qualitative phenomena can be seen, with pitting of the original surface (light blue (a)–(c)), hill and valley formation (yellow/blue (d)–(g)), hill sharpening (orange/red (h)) and finally, nanotendrils growth (red (i)–(j)). Each cell dimension is  $10 \times 10$  nm (initial pit radius  $\sim 10$  nm). The colour scale at bottom also in units of 10 nm.

experimental section. By modelling only the simple assumption that a bubble created in the bulk is more likely to impact in a depressed feature, rather than a raised feature, the pitting density saturation, hill formation and narrowing into tendrils, as well as the areal feature coverage are matched between experiment and model.

Additionally, assuming that the number of bubbles produced is linearly proportional to the fluence at small fuzz thickness results in similar numbers for the fluences at which hills are formed and thin into tendrils when equating 1000 bubbles to a fluence of  $5 \times 10^{25} \text{ m}^{-2}$  (pitting saturation). If all of the helium incident on the sample were in the 10 nm bubbles, this would lead to pressures much higher than the 10s of Gbar

predicted by MD simulations [14]. This discrepancy could be accounted for by annealing of the surface leading to a higher number of bubbles required to create the same morphological changes, or the presence of helium sinks in the material that do not lead to bubble formation (i.e. grain boundaries [19], or helium atom diffusion to the surface).

Finally, it should also be noted here that the hypothesis presented here as well as the model supporting that hypothesis only account for the initial morphological changes. As the fuzz layer continues to grow to thicknesses much greater than the fuzz tendrils diameter, ion implantation should occur primarily in the tendrils rather than the bulk; a complication also alluded to by Kajita [13]. Further growth, however, may be explained by the surface diffusion model proposed by Martynenko [20], and supported by Miyamoto [15].

## References

- [1] Baldwin M.J. and Doerner R.P. 2010 Formation of helium induced nanostructure 'fuzz' on various tungsten grains *J. Nucl. Mater.* **404** 165–73
- [2] Wright G.M. et al 2013 Comparison of tungsten nano-tendrils grown in Alcator C-Mod and linear plasma devices *J. Nucl. Mater.* **438** S84–9
- [3] Brooks J.N., Allain J.P., Doerner R.P., Hassanein A., Nygren R., Rognlien T.D. and Whyte D.G. 2009 Plasma–surface interaction issues of an all-metal ITER *Nucl. Fusion* **49** 035007
- [4] Najmabadi F. and the ARIES Team 2006 The ARIES-AT advanced tokamak. Advanced technology fusion power plant *Fusion Eng. Des.* **80** 3–23
- [5] Takamura S., Ohno N., Nishijima D. and Kajita S. 2006 Formation of nanostructured tungsten with arborescent shape due to helium plasma irradiation *Plasma Fusion Res.* **1** 051
- [6] De Temmerman G., Bystrov K., Zielinski J., Balden M., Matern G., Arnas C. and Marot L. 2012 Nanostructuring of molybdenum and tungsten surfaces by low-energy helium ions *J. Vac. Sci. Technol. A* **30** 041306
- [7] Baldwin M.J. and Doerner R.P. 2008 Helium induced nanoscopic morphology on tungsten under fusion relevant plasma conditions *Nucl. Fusion* **48** 5
- [8] Baldwin M.J., Lynch T.C., Doerner R.P. and Yu J.H. 2011 Nanostructure formation on tungsten exposed to low-pressure rf helium plasmas: a study of ion energy threshold and early stage growth *J. Nucl. Mater.* **415** S104–7
- [9] Ruzic D.N. 1994 *Electric Probes for Low Temperature Plasmas* (New York: American Vacuum Society Education Committee)
- [10] Tobe R., Sekiguchi A., Sasaki M., Okada O. and Hosokawa N. 1996 *Thin Solid Films* **281–282** 155–8
- [11] Baldwin M.J., Doerner R.P., Nishijima D., Tokunaga K. and Ueda Y. 2009 The effects of high fluence mixed-species (deuterium, helium, beryllium) plasma interactions with tungsten *J. Nucl. Mater.* **390–391** 886–90
- [12] Doerner R.P., Baldwin M.J. and Stangeby P.C. 2011 An equilibrium model for tungsten fuzz in an eroding plasma environment *Nucl. Fusion* **51** 043001
- [13] Kajita S., Yoshida N., Yoshihara R., Ohno N. and Yamagiwa M. 2011 TEM observation of the growth process of helium nanobubbles on tungsten: nanostructure formation mechanism *J. Nucl. Mater.* **418** 152–8
- [14] De Temmerman G., Bystrov K., Doerner R.P., Marot L., Wright G.M., Woller K.B., Whyte D.G. and Zielinski J.J. 2013 Helium effects on tungsten under fusion-relevant plasma loading conditions *J. Nucl. Mater.* **438** S78–83

- [15] Miyamoto M., Watanabe T., Nagashima H., Nishijima D., Doerner R.P., Krashennikov S.I., Sagara A. and Yoshida N. 2014 *In situ* transmission electron microscope observations of the formation of fuzzy structures on tungsten *Phys. Scr.* **T159** 014028
- [16] Hu L., Hammond K.D., Wirth B.D. and Maroudas D. 2014 Dynamics of small mobile helium clusters near tungsten surfaces *Surf. Sci.* **626** L21–5
- [17] Sefta F., Juslin N. and Wirth B.D. 2013 Helium bubble bursting in tungsten *J. Appl. Phys.* **114** 243518
- [18] Lasa A., Tahtinen S.K. and Nordlund K. 2014 Loop punching and bubble rupture causing surface roughening: a model for W fuzz growth *Europhys. Lett.* **105** 25002
- [19] El-Atwani O., Efe M., Heim B. and Allain J.P. 2013 Surface damage in ultrafine and multimodal grained tungsten materials induced by low energy helium irradiation *J. Nucl. Mater.* **434** 170–7
- [20] Martynenko Y.V. and Nagel M.Y. 2012 Model of fuzz formation on a tungsten surface *Plasma Phys. Rep.* **38** 996–9